

See discussions, stats, and author profiles for this publication at: <https://www.researchgate.net/publication/233907802>

# Unilateral Access Regulation: Ground State Dynamics of the *Pseudomonas aeruginosa* Outer Membrane Efflux Duct OprM

ARTICLE *in* BIOCHEMISTRY · DECEMBER 2012

Impact Factor: 3.02 · DOI: 10.1021/bi3014714 · Source: PubMed

---

CITATIONS

7

---

READS

31

4 AUTHORS, INCLUDING:



Christian Kandt

Hochschule Bonn-Rhein-Sieg

45 PUBLICATIONS 855 CITATIONS

SEE PROFILE

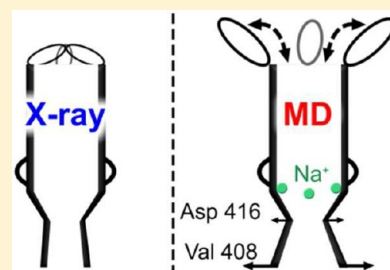
# Unilateral Access Regulation: Ground State Dynamics of the *Pseudomonas aeruginosa* Outer Membrane Efflux Duct OprM

Dennis C. Koch, Martin Raunest, Tim Harder,<sup>†</sup> and Christian Kandt\*

Computational Structural Biology, Department of Life Science Informatics B-IT, Life & Medical Sciences (LIMES) Institute, University of Bonn, Dahlmannstraße 2, 53113 Bonn, Germany

**S** Supporting Information

**ABSTRACT:** Acting as an efflux duct in the MexA–MexB–OprM multidrug efflux pump, OprM plays a major role in the antibiotic resistance capability of *Pseudomonas aeruginosa*, trafficking substrates through the outer cell membrane. Whereas the available crystal structures showed restricted OprM access on both ends, the underlying gating mechanism is not yet fully understood. To gain insight into the functional mechanism of OprM access regulation, we conducted a series of five independent, unbiased molecular dynamics simulations, computing 200 ns dynamics samples of the wild-type protein in a phospholipid membrane/150 mM NaCl water environment. On the extracellular side, OprM opens and closes freely under the simulated conditions, suggesting the absence of a gating mechanism on this side of the isolated protein. On the periplasmic side, we observe an opening of the tip regions at Val408 and to a lesser degree Asp416 located 1.5 nm further into the channel, leading to OprM end conformations being up to 3 and 1.4 times, respectively, more open than the asymmetric crystal structure. If our simulations are correct, our findings imply that periplasmic gating involves only the Asp416 region and that in vivo additional components, absent in our simulation, might be required for periplasmic gating if the observed opening trend near Asp416 is not negligible. In addition to that, we identified in each monomer a previously unreported sodium binding site in the channel interior coordinated by Asp171 and Asp230 whose functional role remains to be investigated.



The aerobic, Gram-negative bacterium *Pseudomonas aeruginosa* is a common pathogen that can be found in almost all kind of environments.<sup>1</sup> Especially for humans with weak immunity or damaged tissue, *P. aeruginosa* can cause severe medical conditions.<sup>2</sup> One of the most troublesome characteristics of *P. aeruginosa* is the strong antibiotic resistance capability that often originates from the expression and activity of multidrug efflux pumps.<sup>3,4</sup>

Until now, several multidrug efflux pump systems have been characterized in *P. aeruginosa*, including the most prominent ones, MexA–MexB–OprM,<sup>5</sup> MexC–MexD–OprJ, MexE–MexF–OprN, and MexX–MexY–OprM.<sup>6–8</sup> Displaying different substrate specificities, these systems extrude a wide range of antimicrobial agents, including quinolones, tetracyclines, and most penicillins.<sup>6</sup> In wild-type cells, the MexA–MexB–OprM system is the only efflux system that is expressed constantly.<sup>9</sup> The corresponding operon encodes MexA, a periplasmic adaptor or membrane fusion protein (MFP), MexB, an inner membrane drug-proton antiporter of the resistance nodulation division (RND) protein superfamily, and the outer membrane factor (OMF), OprM.<sup>10–12</sup> Assembling transiently, these components form a tripartite efflux system with MexB acting as the engine and the active transporter expelling various compounds out of the cell via the outer membrane efflux duct OprM. MexA is assumed to couple MexB and OprM in the assembled pump.<sup>13</sup> Beyond interacting with MexA and MexB, OprM also functions as an efflux duct in conjunction with other inner membrane transporters.<sup>8,14,15</sup>

At present, two OprM crystal structures have been determined, the first of a single monomer<sup>16</sup> and the second of the entire trimer,<sup>17</sup> showing the efflux duct at resolutions of 2.56 and 2.4 Å, respectively. OprM is a homotrimer forming a hollow cylinder and displays a very high degree of conformational similarity to its *Escherichia coli* homologue TolC with an  $\alpha$ -carbon root-mean-square deviation (rmsd) of 1.6 Å despite a low level of sequence identity of 19%.<sup>17</sup> Like TolC, OprM exhibits a  $\beta$ -barrel domain embedded in the outer membrane from which an  $\alpha$ -helical domain extends 100 Å into the periplasmic space. A ringlike equatorial domain surrounds the  $\alpha$ -helical domain's middle section, while the protein's N-terminus is attached to the outer membrane via a palmitoyl lipid anchor (Figure 1A).

Acting as an efflux duct in a transiently assembled transport system, OprM occurs in at least two different states: one permitting and one blocking the passage of substrates. While in the available X-ray structures OprM access is restricted on the extracellular and periplasmic side, the underlying mechanisms of gating and access regulation are not yet fully understood. Similar to TolC, an irislike opening mechanism has been proposed on the periplasmic side,<sup>18</sup> whereas elastic network normal-mode analyses suggested additional conformational changes involving twisting and stretching motions of OprM.<sup>17</sup>

**Received:** October 30, 2012

**Revised:** December 10, 2012

For TolC, recent computer simulations suggested that channel access is regulated only on the periplasmic side in a sodium-dependent manner while on the extracellular side the isolated wild-type protein opens and closes freely.<sup>19</sup>

Addressing the question of OprM access regulation and gating mechanism as well as exploring the potential influence of sodium ions, we conducted a series of five independent, unbiased 200 ns molecular dynamics (MD) simulations of membrane-embedded wild-type OprM in a 150 mM NaCl solution. On the extracellular side, we find OprM opening and closing freely, suggesting the absence of a gating mechanism on this side in the isolated protein. Assuming a similar architecture as in its *E. coli* homologue TolC, comprising an inner and outer bottleneck region, we monitored OprM's periplasmic opening state using Asp416 and Val408, which we selected on the basis of their proximity to their TolC counterparts after the superimposition of OprM and TolC X-ray structures. In all simulations, an opening of both bottlenecks occurs. However, the effect is more strongly pronounced in the outer bottleneck region, reaching end conformations up to 3 times more open than the starting crystal structure. At the same time, the inner bottleneck displays postsimulation conformations only 1.1–1.4 times more open than in the starting structure. If our simulations are correct, our findings imply that periplasmic gating occurs only in the inner bottleneck region at Asp416 and that in vivo additional components, absent in our simulation, might be required for periplasmic gating if the observed opening trend at Asp416 is not negligible. In addition to that, we identified in each monomer a previously unreported sodium binding site in the channel interior coordinated by Asp171 and Asp230. Apparently uninvolved in gating or structural stabilization, the functional role of the Na site remains to be investigated.

## EXPERIMENTAL PROCEDURES

**Molecular Dynamics Simulations.** MD simulations were performed employing GROMACS version 4.0.3<sup>20,21</sup> and the GROMOS96-53a6 force field<sup>22</sup> using the 3DSK OprM crystal structure<sup>17</sup> as a starting structure. The protein was inserted in a pre-equilibrated 9.6 nm × 9.6 nm palmitoylcholinephosphatidylethanolamine (POPE) bilayer patch<sup>23</sup> using INFLATEGRO.<sup>24</sup> The system was solvated with simple point charge water molecules<sup>25</sup> and 181 Na<sup>+</sup> and 166 Cl<sup>−</sup> ions, yielding a 150 mM NaCl solution and a total system charge of zero (Figure 1A). Standard protonation states were assumed for titratable residues. After a 20 ns membrane equilibration with protein atoms position-restrained using a force constant of 1000 kJ mol<sup>−1</sup> nm<sup>−2</sup>, five independent MD runs with different starting velocities were performed, each 200 ns in length.

In the simulations, all bond lengths were constrained by LINCS<sup>26</sup> so that an integration time step of 2 fs could be chosen. Systems were simulated at 310 K, maintained separately for protein, lipids, and water by a Berendsen thermostat<sup>27</sup> with a time constant ( $\tau_T$ ) of 0.1 ps. Pressure coupling was done employing a Berendsen barostat<sup>27</sup> using a 1 bar reference pressure and a time constant of 4 ps. Semi-isotropic pressure coupling was employed to permit bilayer fluctuations in the membrane plane. Electrostatic interactions were calculated using particle mesh Ewald (PME) summation,<sup>28,29</sup> and twin range cutoffs of 1.0 and 1.4 nm were applied for computing the van der Waals interactions.

**Analysis.** To monitor protein stability and conformational drift throughout the simulations, we computed *Ca* rmsds after

least-squares fitting to the starting structure (Figure 1). This was done for the entire protein as well as the transmembrane  $\beta$ -barrel, including the extracellular loops, the  $\alpha$ -helical domain, the equatorial domain, and the membrane-anchoring N-terminus. To assess the overall amount of conformational sampling throughout the simulation, a principal component analysis was performed on the  $\alpha$ -carbon trajectories of all simulations.

As in ref 19, the OprM opening state on the extracellular side was monitored through dihedral angle  $\theta$  spanned by the *Ca* atoms of Ser113 located in the  $\beta$ -barrel and Thr106 at the tip of each extracellular loop (Figure 2A). As the outwardly closed 3DK5 crystal structure displays an average  $\theta$  value of 99.6° (Figure 2D), an extracellular loop was regarded as closed as or more closed than 3DSK whenever  $\theta \leq 100^\circ$ . Conversely, a loop for which  $\theta > 100^\circ$  was considered more open than the 3DSK X-ray structure. In each simulation,  $\theta$  was monitored for each extracellular loop (Figure 2B1) and subsequently converted to a binary representation of “more open” than 3DSK (a value of 0) or “more closed” (assigned a value of 1) (Figure 2B2). As a summary for each run, the number of loops in the closed conformation was determined (Figure 2B3) and converted to a frequency histogram (Figure 2B4) reflecting for each simulation the percentage occurrence of closed loop conformations (Figure 2C). To obtain an overview of the extracellular loop conformations visited throughout all simulations, we calculated a histogram showing the  $\theta$  distribution in all five runs (Figure 2D).

As in refs 19 and 30, the periplasmic OprM opening state was monitored through  $\alpha$ -carbon triangular cross-sectional area (TCA) analysis (Figure 3). The corresponding Asp416 and Val408 OprM residues representing the inner (BNI) and outer periplasmic bottleneck (BNII) were selected on the basis of their average minimal  $\alpha$ -carbon distance to their TolC counterparts, Asp374 (1.97 Å) and Gly365 (2.36 Å),<sup>31,32</sup> after superimposition of the 3DSK and 1EK9 OprM and TolC crystal structures using PyMol 1.5<sup>33</sup> (Figure 3A).

To analyze the distribution of sodium throughout the simulations, both one-dimensional (1D) Na<sup>+</sup> density profiles along the membrane normal and average spatial sodium distributions were computed. The former was done using the GROMACS tool *g\_density*, and for the latter, we employed the VolMap function in VMD version 1.9<sup>43</sup> using a spatial resolution of 1 Å<sup>3</sup> to analyze the distribution of sodium at four density levels ranging from 0.01 to 0.8 Na<sup>+</sup>/Å<sup>3</sup>. Sodium binding and unbinding were monitored analyzing the *z*-coordinate trajectory of each Na<sup>+</sup> ion and computing for each OprM monomer the percentage of simulation time a residue comes into contact with at least one sodium ion in at least one monomer. For this analysis, we employed a residue–Na distance cutoff of  $\leq 3$  Å. Both the sodium distributions and the residue contact analyses were performed for all five simulations. To quantify sodium occupation of the detected interaction site, we calculated the run and time-averaged percentage of simulation time during which one, two, or three sodium ions are simultaneously present within 3 Å of Asp171 and Asp230.

As described in ref 34, simulation average structures were calculated using an iterative scheme of calculating the average conformation and realigning the trajectory to that average structure before computing a new average structure. This procedure was repeated until the average structure stopped changing.

## RESULTS

**Protein Stability and Conformational Sampling.** To monitor protein stability and conformational drift, we computed for each simulation the  $C\alpha$  rmsds for the whole protein, the  $\beta$ -barrel, including the extracellular loops, the  $\alpha$ -helical domain, the equatorial domain, and the membrane-anchoring N-terminus (Figure 1B). With rmsds ranging from 4

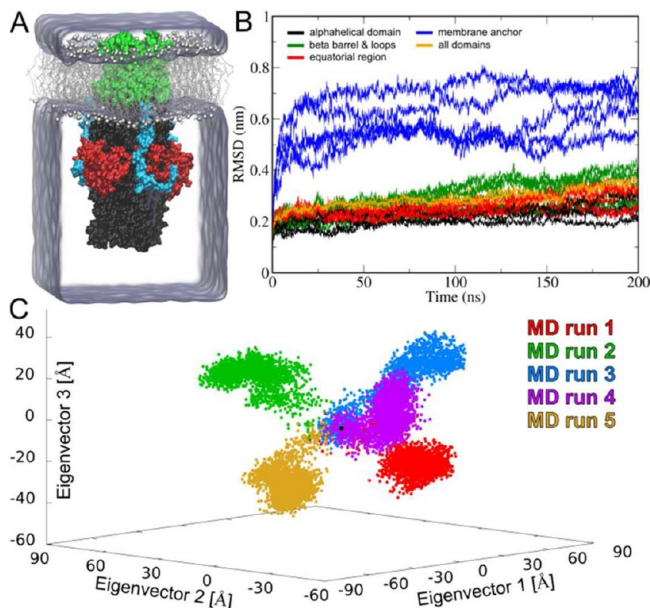


**Figure 1.** (A) Molecular dynamics simulations of wild-type 3DSK OprM conducted in a POPE phospholipid/150 mM NaCl water environment. The coloring scheme represents different OprM regions: green for  $\beta$ -barrel and extracellular loops, black for the  $\alpha$ -helical domain, red for the equatorial domain, and blue for the membrane-anchoring N-terminus. (B)  $C\alpha$  root-mean-square deviations after respective least-squares fitting to the starting structure. While the largest conformational changes occur in the membrane-anchoring N-termini and the  $\beta$ -barrel–extracellular loop region, the overall rmsds of the entire protein are still increasing after 200 ns. (C) To assess the amount of conformational sampling during our simulations, we conducted a principal component analysis mapping for each simulation of OprM’s path through conformational space down to the three dimensions spanned by the first three eigenvectors.

to 8 Å, the largest conformational changes occurred in the membrane-connecting N-terminal regions followed by the  $\beta$ -barrel–extracellular loop regions displaying rmsds of up to 4.5 Å. For the equatorial and  $\alpha$ -helical domains, we observed rmsd ranges of 2–3.5 and 1.5–3 Å, respectively. As indicated by the continuously increasing rmsd curves of the entire protein, within the simulation time of 200 ns, no stable rmsd plateaus are reached. Assessing the overall amount of conformational changes during our simulations, we conducted a principal component analysis of the concatenated  $C\alpha$  trajectories. Projecting OprM’s pathway onto the first three eigenvectors, we find that in each run the protein explores different regions of conformational hyperspace around the X-ray structure (Figure 1C).

**Gating. Extracellular Side.** To analyze the extracellular opening state of OprM, we monitored dihedral angle  $\theta$  formed by the  $C\alpha$  atoms of Ser113 in the  $\beta$ -barrel and Thr106 at the tip of each extracellular loop. Using the 3DSK X-ray structure’s average  $\theta$  dihedral of 100° as a reference, loop conformations

were classified as “closed or more closed” than the crystal structure when  $\theta \leq 100^\circ$ , whereas loop conformations with  $\theta > 100^\circ$  were regarded as “more open” than the 3DSK X-ray structure. Throughout the simulations, we observed a variety of extracellular loop conformations ranging from zero to three closed loops (Figure 2E), whereas the highest frequency was found to be in the range of zero closed loops. Whereas the overall  $\theta$  distribution calculated over all simulations ranges from 30° to 165°, displaying a maximum at 120° (Figure 2D), the 1WP1 and 3DSK crystal structures show average  $\theta$  values of ~105° and 100° (Figure 2D).

**Periplasmic Side.** Monitoring the OprM opening state on the periplasmic side, we calculated the triangular cross-sectional area (TCA) rendered by the  $C\alpha$  atoms of Asp416 and Val408 representing the inner (BNI) and outer periplasmic bottleneck (BNII) (Figure 3A). In all five simulations, the outer bottleneck BNII consistently opens up during the first 100 ns (Figure 3B), reaching TCAs in the range of  $206.1 \pm 45.5 \text{ Å}^2$  with a maximum of  $351.9 \text{ Å}^2$  after 165.8 ns in run 2 (Figure 3D). The corresponding TCAs of starting structure 3DSK (Figure 3C) and the 1WP1 crystal structure (Figure 3E) amount to 83.9 and  $125.3 \text{ Å}^2$ , respectively. If one starts from a TCA of  $59.4 \text{ Å}^2$  in the 3DSK crystal structure, the inner bottleneck BNI also shows a slight opening trend leading to a TCA range from 60 to  $84 \text{ Å}^2$  by the end of the simulations. A summary of the average, minimal, and maximal opening states of the inner and outer periplasmic bottleneck compared to the 1WP1 and 3DSK crystal structures is given in Table 1. Computing Connolly surfaces with different probe sphere radii, we found that the 3DSK X-ray structure is sterically permeable for molecules with a diameter of  $\leq 1.2 \text{ Å}$ , whereas the maximal BNI opening observed in one simulation at 107 ns permits the passage of molecules with a diameter of  $\leq 6.4 \text{ Å}$ .

**Sodium Distributions and Binding Sites.** Computing time-averaged 1D  $\text{Na}^+$  density profiles along the  $z$ -axis, sodium  $z$ -trajectories, and time- and run-averaged spatial  $\text{Na}^+$  density distributions, we searched for potential OprM sodium binding sites similar to those recently described for TolC.<sup>19</sup> Next to the lipid headgroups, the 1D  $\text{Na}^+$  density profiles indicate a site of heightened sodium density in the lower equatorial region of the channel (Figure 4A) continuously occupied throughout the entire simulation time, which is made evident by a stable sodium trace in the  $\text{Na}^+$   $z$ -trajectory representatively shown for MD run 1 (Figure 4B). Zooming in on the individual sodium ions contributing to this trace, we find that once initial binding has occurred (during the first 5–40 ns), all three binding sites remain occupied but not by the same individual  $\text{Na}^+$  ions as these exchange in all simulations (Figure 1 of the Supporting Information). Spatial sodium distributions in this region display maxima in sodium density exceeding  $0.8 \text{ Na}^+/\text{Å}^3$  near Asp171, Asp230, and Leu226 in each monomer (Figure 4C). Counting the number of  $\text{Na}^+$ –residue contacts within 3 Å, we found that sodium predominantly interacts with Asp171 and Asp230, exhibiting run-averaged contact frequencies of 78 and 77%, respectively, of the simulation time (Figure 4D). Calculating the number of sodium ions simultaneously located within 3 Å of Asp171 and Asp230, we find single occupation of the  $\text{Na}^+$  interaction site being the predominant form, exhibiting run- and time-averaged residence frequencies of 88% in monomers A and B as well as 89% in monomer C (Table 2).

To gain insight into the structural basis underlying the different sodium binding sites observed for OprM and TolC,<sup>19</sup> we compared the channel internal distribution of Asp and Glu



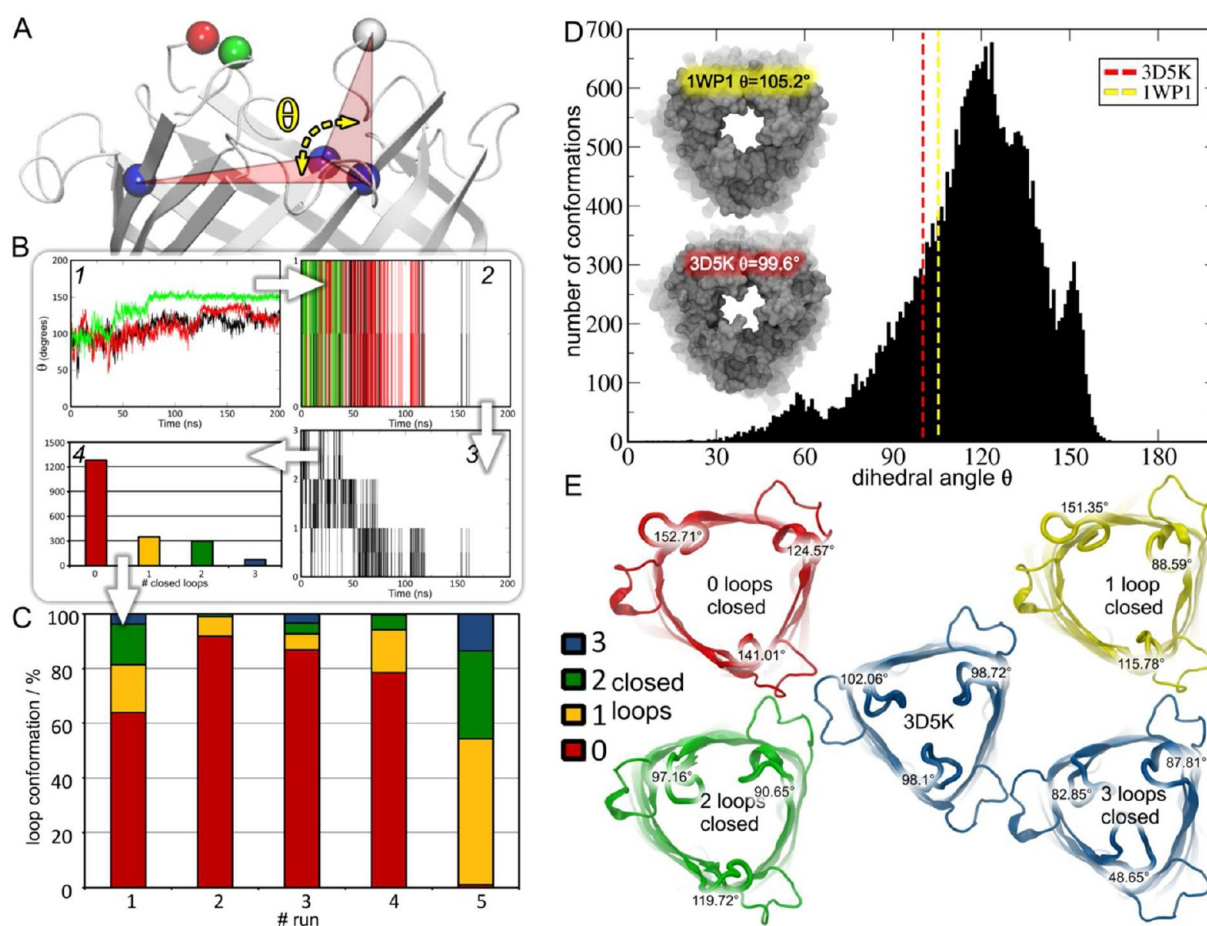


**Figure 2.** (A) On the extracellular side, the OprM opening state was monitored through dihedral angle  $\theta$  formed by the  $\alpha$ -carbons of Ser113 in the  $\beta$ -barrel and Thr106 at the tip of each extracellular loop. (B) As the outwardly closed 3D5K crystal structure displays an average  $\theta$  value of 99.6°, an extracellular loop was regarded as closed as or more closed than 3D5K whenever  $\theta \leq 100^\circ$ . In each simulation,  $\theta$  was monitored for each extracellular loop (1) and subsequently converted to a binary representation of “more open” than 3D5K (assigned a value of 0) or “more closed” (assigned a value of 1) (2). As a summary for each run, the number of loops in the closed conformation was determined (3) and converted to a frequency histogram (4), reflecting for each simulation the number of closed extracellular loops and the percentage of simulation time spent in that conformation (C). As shown by the overall  $\theta$  distribution calculated over all runs (D) and simulation snapshots and the 3D5K crystal structure (E), the extracellular loops adopt a broad range of conformations, preferring the completely open state under the simulated conditions (C and D).

residues in the 3D5K OprM and 1EK9 TolC crystal structures (Figure 5). In both cases, *in silico* sodium binding is restricted to regions where two aspartates are located in the proximity of each other such as Asp374 and Asp371 in TolC’s periplasmic bottleneck or Asp171 and Asp230 near the inward-facing side of the equatorial domain in OprM.

**Simulation versus X-ray.** Throughout our simulations, wild-type OprM adopts conformations on the extracellular (Figure 2) and periplasmic side (Figure 3) that have not been reported in the published crystal structures.<sup>16,17</sup> To provide possible evidence explaining this discrepancy, we calculated the simulation average structure over all five simulations and compared it to the 3D5K X-ray structure (Figure 6). As indicated by superposition of the simulation average and X-ray structure after  $C\alpha$  least-squares fitting (Figure 6A) and calculation of  $C\alpha$  displacements for each monomer (Figure 6B), with an overall rmsd of 1.98 Å, the conformational differences are small and the largest deviations occur in membrane-connecting N-termini, the extracellular loop, and the periplasmic tip regions. In particular, residues at the periplasmic tip region exceeding  $C\alpha$  displacements of 3 Å (colored cyan in Figure 6C) partially coincide with 4 Å crystal

contacts (van der Waals representation in Figure 6C) in the 3D5K X-ray structure. Additionally, we have analyzed the crystallographic  $B$  factors of the OprM crystal structures by plotting their  $C\alpha$  root-mean-square fluctuations along the membrane normal (Figure 7). Both X-ray structures display flexibility patterns with maxima of root-mean-square fluctuations occurring at the extracellular and periplasmic end of the protein.

## DISCUSSION

In this study, we report a series of five independent, unbiased 200 ns MD simulations of wild-type OprM in a phospholipid membrane/150 mM NaCl water environment, addressing the question of access regulation. On the extracellular and periplasmic side, OprM visits conformations throughout the simulations that have not been observed in the available OprM crystal structures. While we observed free opening and closing on the extracellular side, we observed on the periplasmic side an opening of the outer periplasmic bottleneck region (BNII) monitored at Val408. At the same time, the inner periplasmic bottleneck (BNI) monitored through Asp416 shows a slighter opening trend restricting passage to molecules with a maximal

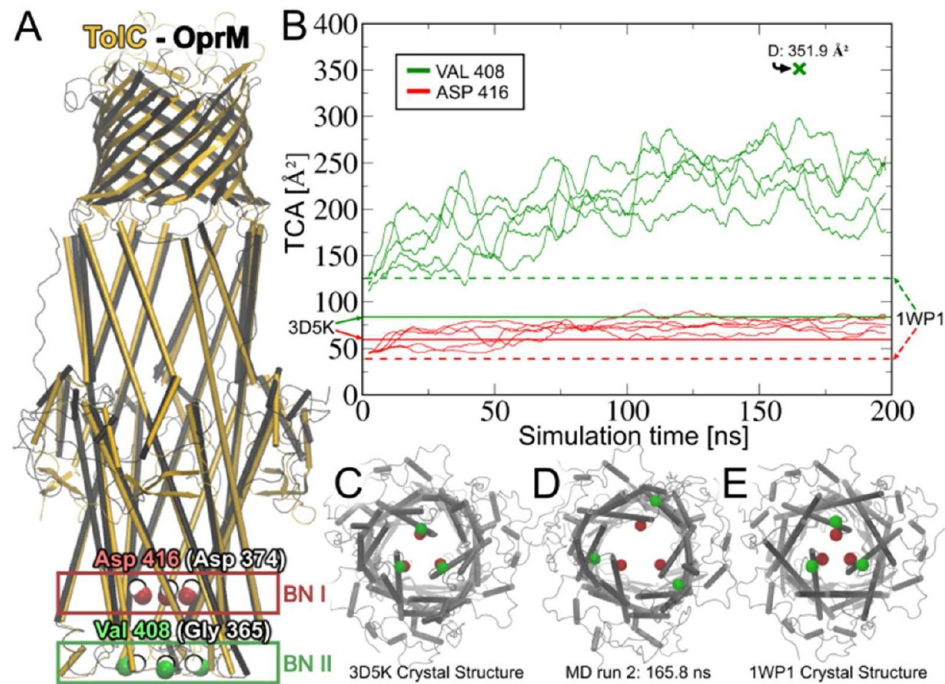


**Figure 3.** (A) On the periplasmic side, the OprM opening state was monitored using the triangular cross-sectional area (TCA) spanned by the  $\alpha$ -carbons of Asp416 and Val408, representing an inner (BNI) and outer periplasmic bottleneck (BNII) based on the proximity of the residues to their TolC counterparts, Asp374 and Gly365, respectively. (B) Both bottlenecks open during the simulations; however, in BNII, the opening is more strongly pronounced, leading to TCAs up to 3 times higher than in the 3D5K starting structure by the end of the simulations, whereas BNI is only 1.1–1.4 times more open after 200 ns. (C–E) Conformational snapshots illustrate periplasmic OprM conformations in the asymmetric (C) and symmetric crystal structure (E) as well as at maximum BNII opening (D). For the sake of clarity, the TCAs have been smoothed using a running average filter of 5 ns. Bold crosses mark the unfiltered TCA maxima.

**Table 1. OprM Periplasmic Opening States As Observed in the Crystal Structures and Our Molecular Dynamics Simulations**

OprM structure	outer periplasmic bottleneck Val408 (BNII)		inner periplasmic bottleneck Asp416 (BNI)	
	av TCA (Å <sup>2</sup> )	av C $\alpha$ distance (Å)	av TCA (Å <sup>2</sup> )	av C $\alpha$ distance (Å)
3D5K	83.9	13.9	59.4	11.7
1WP1	125.3	17	38.7	9.5
simulation	206.1 $\pm$ 45.5	21.9 $\pm$ 3	69.7 $\pm$ 11.3	12.7 $\pm$ 1.4
maximum	351.9	31.1	103.6	18.1
minimum	85.4	12	39.4	8.6

diameter of 6.4 Å. In addition to that, we report a new sodium binding site at Asp171 and Asp230 located inside the OprM channel near the lower, periplasm-facing equatorial domain of the protein. We start this section discussing the limitations of our approach and then proceed to our findings and their biological implications.

**Limitations of Our Approach.** The microenvironment of OprM in the outer membrane of *P. aeruginosa* is characterized by a variety of different lipids and membrane proteins,<sup>35</sup> and whereas the extracellular side of OprM is exposed to lipopolysaccharides in the outer membrane leaflet, the periplasmic side is in contact with the peptidoglycan layer.<sup>36</sup> In contrast to these in vivo conditions, in silico we reduced the microenvironment to a simple POPE bilayer omitting a representation of the peptidoglycan layer. While including both components in simulation studies would certainly be desirable, the development of the appropriate lipopolysaccharides and peptidoglycan molecular topologies is still in its

infancy,<sup>37–39</sup> and at present, such simulation parameters were not yet available for *P. aeruginosa*. On the other hand, our choice of a simple uniform membrane model excluding the peptidoglycan and other components is also justified by other simulation studies of outer membrane proteins making biologically relevant predictions using similar simplifications.<sup>19,40–42</sup> Whereas one could argue that the OprM behavior we observe on the extracellular side could be an artifact of our simplified membrane model, it is encouraging that one of the first lipopolysaccharide simulations that aimed to examine the outer membrane protein OprF<sup>39</sup> reported that the lipopolysaccharides have a stabilizing effect on the open conformation of the OprF extracellular loops that exhibit an architecture similar to that in OprM.

With any molecular dynamics study, the question of whether the simulation length is appropriate for the problem under investigation arises. In light of recent findings of atomistic membrane protein simulations showing that neither 300 ns TolC<sup>19</sup> nor 1600 ns rhodopsin MD simulations<sup>43</sup> were long enough for the protein structure to converge, our observation that OprM's C $\alpha$  rmsds still increase after 200 ns (Figure 1B) is not surprising. With OprM sampling different regions of conformational space in each run (Figure 1C), the protein structure has clearly not yet equilibrated, underscoring the need for long duration simulations. However, our study's focus is on exploring wild-type OprM ground state dynamics near the X-ray structure and the simulated 200 ns time scale on which the protein already displays unreported conformations (Figures 2 and 3) and ion interaction (Figure 4, Figure 1 of the Supporting Information), which might provide potential new insight into the OprM functional mechanism as discussed



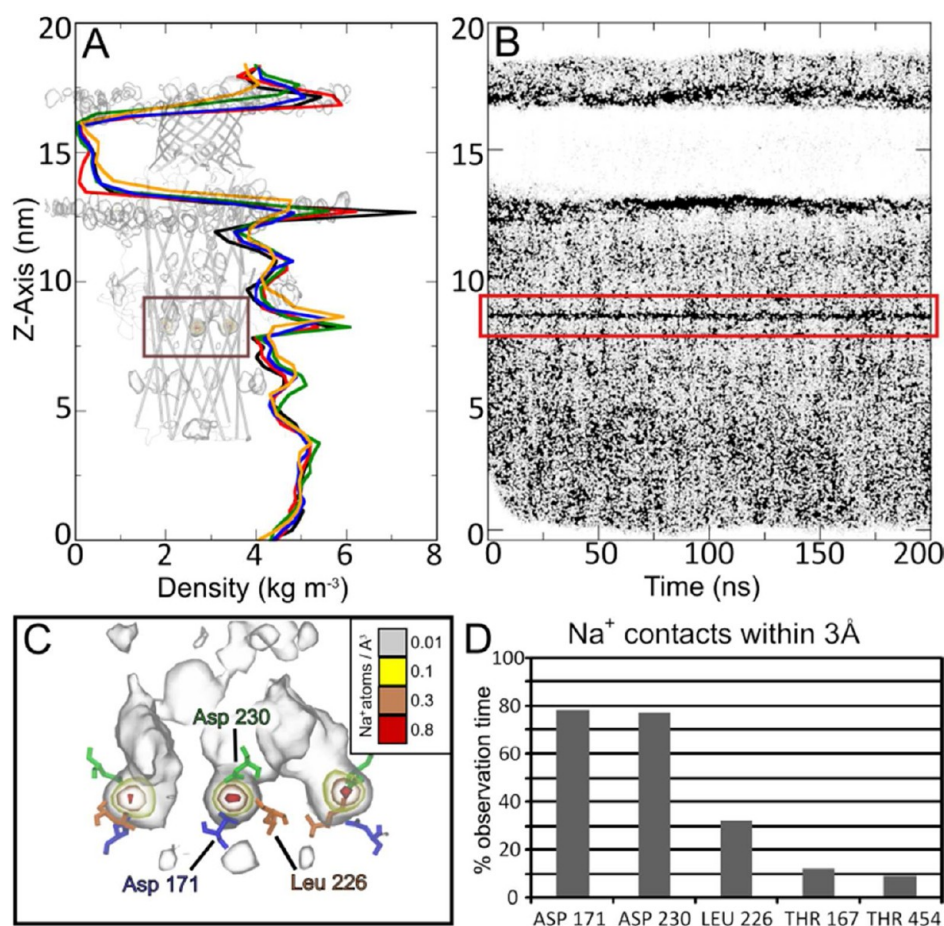


**Figure 4.** Sodium distribution and interaction sites. (A) Partial sodium densities calculated for all simulations indicate the presence of two preferred sodium binding sites: at the lipid headgroups and in the lower equatorial region of the OprM channel. (B) The protein site is continuously occupied for the entire simulation time as indicated by a stable sodium trace in a Na<sup>+</sup> z-trajectory plot shown representatively for run 1. (C) Run- and time-averaged spatial sodium distributions in the lower equatorial region show for each monomer maxima in Na<sup>+</sup> density in the channel interior near Asp171, Asp230, and Leu226 which we find interacting with sodium for 78, 77, and 32%, respectively, of the simulation time at a distance of  $\leq 3$  Å (D).

**Table 2. Run- and Time-Averaged Occupancy (percent) of the Detected Asp171 and Asp230 Sodium Interaction Sites Using a Distance Cutoff of 3 Å**

no. of Na <sup>+</sup> ions	monomer A	monomer B	monomer C
0	10.8	10.6	10.1
1	88.3	88.4	88.9
2	0.9	1.0	1.0
3	0	0	0

below. In that light, we consider the amount of conformational sampling achieved in our simulations adequate for the purpose of this investigation, providing the first samples of membrane-embedded OprM dynamics in atomistic detail.

**Simulation versus X-ray.** Undergoing opening and closing motions on the extracellular side (Figure 2) as well as opening on the periplasmic side in the Val408 region and to a lesser extent in the Asp416 region (Figure 3), wild-type OprM adopts conformations throughout our simulations that have not been reported in the available crystal structures.<sup>16,17</sup> A possible explanation for why these conformations have not been detected yet could be that the crystal environment sterically hinders the conformational changes we observe. This hypothesis is supported by the distribution of 4 Å crystal contacts in the 3DSK X-ray structure (Figure 6C), coinciding

particularly on the periplasmic side with residues where the conformational differences between the simulation average and crystal structure are maximal (Figure 6B,C). Furthermore, with an overall  $\alpha$  rmsd of 1.98 Å, the conformational difference between the simulation average and crystal structure is small, suggesting that as shown by the results described in refs 19 and 44 the crystal might already contain the open and closed OprM conformations we observe in our simulations. In that case, these conformations either constitute only a minority of the conformational ensemble in the 3DSK OprM crystal or on average are canceling each other out. Either way, the *B* factor distributions in the 100 K<sup>17</sup> and 90 K<sup>16</sup> OprM crystal structures (Figure 7) already imply a heightened degree of flexibility or crystal disorder on the extracellular and periplasmic side of the protein.

**Extracellular Access.** Whereas the available structural data<sup>16,17</sup> suggest that OprM access is restricted on both sides, our findings imply that OprM gating takes place only on the periplasmic side (Figure 3), with OprM opening and closing freely on the extracellular side (Figure 2), suggesting here the absence of a gating mechanism in the isolated wild-type protein. Similar to our previous findings on the OprM homologue TolC,<sup>19</sup> the broad range of extracellular loop conformations visited throughout our simulations includes conformations both

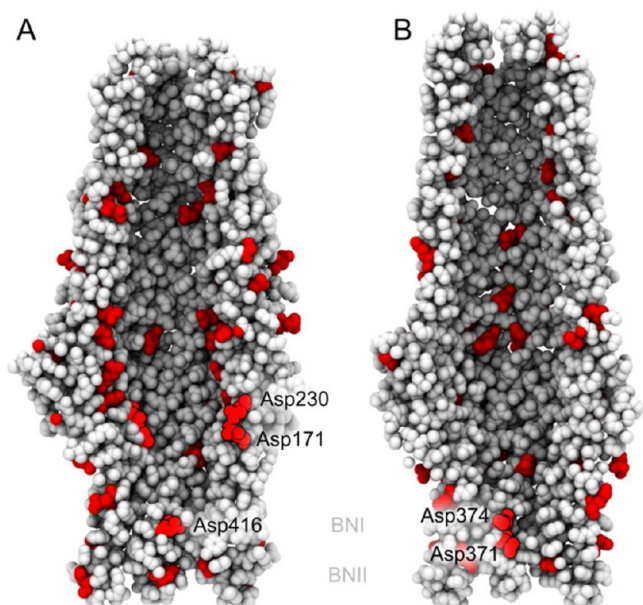


**Figure 5.** Distribution of aspartate and glutamate (red) in the 3D5K OprM (A) and 1EK9 TolC (B) crystal structures. For a better view of the channel interior, both proteins are shown in a cutaway representation. Aspartates constituting the inner bottleneck (BNI) (Asp416 in OprM and Asp374 in TolC) or involved in sodium binding (Asp171 and Asp230 in OprM and Asp374 and Asp371 in TolC) are colored bright red.

more closed and more open than the available X-ray structures<sup>16,17</sup> (Figure 2D,E). As indicated by the distribution of  $\theta$  dihedral angles that we used to monitor the extracellular loops' opening state (Figure 2C), with average  $\theta$  dihedrals of 100 and 105°, the X-ray conformations likely represent only a small section of possible loop conformations compared to the  $\theta$  range of 30–160° we observe in our MD simulations. Whereas the OprM crystal structures limit extracellular access to compounds with diameters of up to 8–10 Å (which we estimated by computing Connolly surfaces using different probe sphere radii), we find that OprM accessibility is sterically only limited by the inner diameter of the  $\beta$ -barrel itself when all three loops are open (Figure 2E). If our simulations of the isolated protein are correct, these results could either indicate the presence of additional gating mechanisms in vivo or hint at the possibility of designing a novel group of OprM-directed drugs specifically targeting the protein interior. Possible

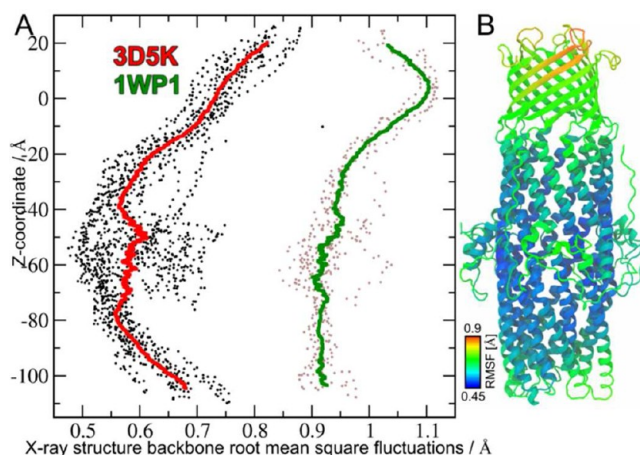


**Figure 7.** Crystal structure flexibility. Using the crystallographic B factors, the backbone root-mean-square fluctuations of the OprM crystal structures are shown as a profile along the membrane normal (A) as well as mapped onto the protein structure in the case of asymmetric 3D5K that we used as the starting structure for our simulations (B).

experimental scenarios for testing the hypothesis of extracellular OprM accessibility could involve double-spin-label electron spin resonance spectroscopy experiments measuring the distance between the tip regions of the extracellular approach. Another approach could be fluorescence spectroscopy experiments in which first a fluorescence dye-specific cross-linker is introduced into the OprM interior and then fluorescence activity is checked after the external application of dyes of different sizes followed by protein extraction and purification. Beyond that, the extracellular accessibility behavior we observe for OprM bears a striking similarity to our previous findings for its *E. coli* homologue, TolC,<sup>19</sup> displaying the same unrestricted opening and closing motions on the extracellular side. In that light, one could hypothesize that unregulated extracellular access might represent a general characteristic shared by all similarly structured efflux ducts. It will be interesting to see this possibility investigated further in future wet lab and computer experiments.

**Periplasmic Access and Sodium Binding Sites.** Whereas for the OprM *E. coli* homologue TolC combined mutagenesis–conductance experiments<sup>31,32</sup> as well as wild-type and mutant crystal structures<sup>45,46</sup> indicated the existence of an inner (BNI) and outer periplasmic bottleneck (BNII), to

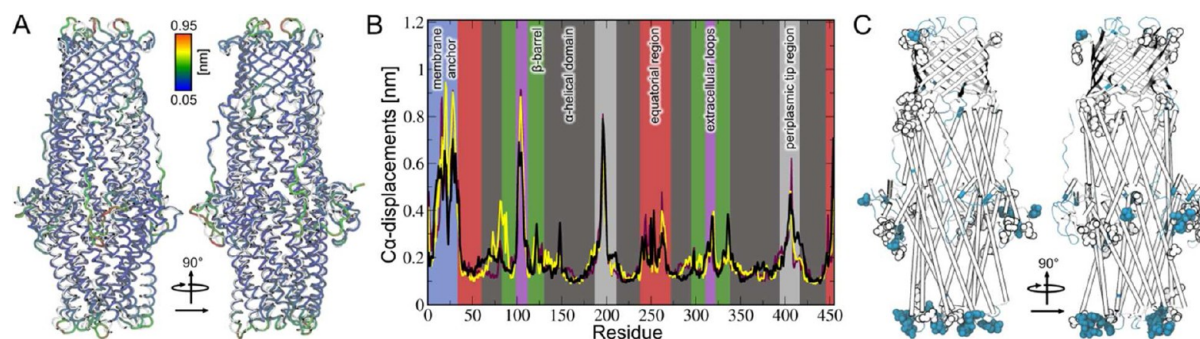


**Figure 6.** (A) Superposition of the 3D5K OprM crystal structure (white) and the simulation average structure calculated over all simulations and colored by  $\text{Ca}$  displacement. (B)  $\text{Ca}$  displacement graphs for each monomer indicate that the largest conformational differences occur in the extracellular loops, the periplasmic tips, and the membrane anchor region. (C) Residues with  $\text{Ca}$  displacements larger than 3 Å (dark cyan) partially coincide with 4 Å crystal contacts (van der Waals representation) in the 3D5K X-ray structure.



the best of our knowledge corresponding investigations of OprM have not yet been reported. Given that (a) in TolC Asp374 and Gly365 have been used to monitor the opening states of the periplasmic bottlenecks<sup>19,30,45</sup> and (b) the OprM structure is very similar to the TolC structure<sup>17</sup> (Figure 3A), we monitored OprM's periplasmic opening state using Asp416 (BNI) and Val408 (BNII) as these residues display the shortest distance to their TolC counterparts after the superimposition of the OprM 3DSK and TolC 1EK9 wild-type crystal structures (Figure 3A). The following section is based on the assumptions that OprM, too, contains two periplasmic bottlenecks and Asp416 and Val408 are appropriate residues for monitoring the bottlenecks' respective opening states.

Whereas in TolC BNI and BNII display similar opening states in the wild-type X-ray structures,<sup>47</sup> inner and outer periplasmic bottlenecks already differ by 21 and 41 Å<sup>2</sup> TCA, respectively, in the symmetric 1WP1 and asymmetric 3DSK OprM crystal structures.<sup>16,17</sup> Throughout our simulations, that difference becomes more pronounced in all runs (Figure 3 and Table 1). BNII opens up in all simulations, reaching TCA values 2.08–2.98 times higher than in the 3DSK starting structure by the end of the simulations. BNI on the other hand also displays an opening trend, albeit much less pronounced, resulting in 1.08–1.4 times higher TCA values after 200 ns. At the same time, we observe in all runs the occurrence of a previously unreported sodium binding site located inside the OprM channel near the equatorial domain where in each monomer the site is predominantly occupied by a single Na<sup>+</sup> ion coordinated by Asp171 and Asp230 (Figure 4, Figure 1 of the Supporting Information, and Table 2).

If our simulations are correct, the observed BNII and BNI behavior could be interpreted in a manner similar to that used for our previous findings on TolC<sup>19</sup> insofar that OprM gating on the periplasmic side involves only the inner but not the outer bottleneck. Moreover, the open BNII conformation could play a role in the formation of the functional complex, initiating interaction with the inner membrane transporter or the adaptor protein. Although not observed throughout the simulations, BNII closure in isolated OprM, sodium-induced as seen for TolC<sup>19</sup> or otherwise, cannot be excluded on the basis of the available data. Confining the BNII opening state by cross-linking and subsequent OprM activity measurements could be one way to investigate this aspect experimentally.

Whether the slight BNI opening trend of a 5–24 Å<sup>2</sup> increase in TCA is negligible or a relaxation effect or represents the beginning of a longer conformational transition inducing a periplasmic opening cannot be decided on the basis of our simulation data alone. However, the two available OprM crystal structures already displaying a much higher variation in the bottlenecks' opening state than the corresponding TolC structures could be interpreted as hinting at a principal functional difference between the two proteins. If the observed BNI opening trend is negligible, this would favor isolated OprM capable of gating when reconstituted in a POPE environment. If the BNI opening trend is not negligible, it seems reasonable to assume that periplasmic OprM access regulation requires an additional component that is absent in our simulations. Electrophysiological conductance experiments with isolated OprM could shed some light on this question. Either way, additional experiments that could involve approaches similar to those used for TolC are required to gain deeper insight into the OprM gating and functional mechanism<sup>31,32</sup> complemented by double-spin-label EPR or

fluorescence spectroscopy studies to monitor and quantify the OprM opening state on the periplasmic side.

Partial and spatial density analysis indicates for each monomer the presence of a so far unreported sodium binding site coordinated by Asp171 and Asp230 (Figure 4 and Figure 1 of the Supporting Information). Unlike our previous findings on TolC,<sup>19</sup> our OprM data do not support an involvement of the sites in a Na<sup>+</sup>-dependent periplasmic lock mechanism as only low Na<sup>+</sup> densities are observed in the bottleneck region and the removal of all NaCl does not alter OprM's periplasmic opening behavior or lead to changes in the protein dynamics or conformation on a 200 ns time scale (data not shown). OprM's insensitivity to NaCl also speaks against a structure stabilizing function of the three Na<sup>+</sup> sites as does the lack of electron density data in the OprM crystal structures in the region of the identified sites that could be interpreted as bound sodium.<sup>17</sup> Two possible explanations can account for the different sodium interactions we observed for OprM and TolC. Either both proteins share a sodium-dependent lock mechanism, or they employ different means of periplasmic access regulations. Given that each MD simulation is always limited by the amount of conformational sampling achieved, the instance that we did not observe any TolC-like sodium binding in OprM's periplasmic bottleneck region does not rule out the possibility that OprM and TolC employ a similar gating mechanism. Longer simulation times might very well yield a different picture than our 200 ns samples. However, spontaneous sodium binding does occur in all our OprM runs too, albeit at a different position, which is evidence of an adequate length of simulation time. Given the different distributions of negatively charged residues in the OprM and TolC channel interior and the observation that *in silico* sodium binding in OprM and TolC is restricted to neighboring aspartates (Figure 5), of which TolC exhibits one near the BNI region and OprM near the inward-facing side of the equatorial domain, it appears reasonable to assume that despite their structural similarity OprM and TolC are indeed different, employing different means of periplasmic access regulation. In both cases, more experimental work is needed to further elucidate the functional mechanism of efflux duct gating and the role of the potential sodium or comparable cation binding sites, for example, activity assays comparing wild-type and mutant OprM under different ionic conditions.

## CONCLUSIONS

To gain insight into the OprM functional mechanism of gating and access regulation, we computed 200 ns dynamics samples of the wild-type protein in a phospholipid membrane/150 mM NaCl water environment in a series of five independent and unbiased atomistic molecular dynamics simulations. On the extracellular side, we find OprM opening and closing freely in all runs, suggesting the absence of a gating mechanism on this side in the isolated protein. Assuming a similar architecture as in its *E. coli* homologue TolC, comprising an inner and outer bottleneck region, we monitored OprM's periplasmic opening state using Asp416 and Val408, which we selected on the basis of their proximity to their TolC counterparts after the superimposition of OprM and TolC X-ray structures. In all simulations, an opening of both bottlenecks occurs, though it is more pronounced in the outer bottleneck region reaching end conformations up to 3 times more open than the starting crystal structure, while the inner bottleneck is only 1.1–1.4 times more open by the end of the simulations. If our simulations are correct, our findings imply that periplasmic

gating occurs only in the inner bottleneck region at Asp416 and that in vivo additional components, absent in our simulations, might be required for gating if the observed opening trend of the inner bottleneck is not negligible. In addition to that, we identified in each monomer a previously unreported sodium binding site in the channel interior coordinated by Asp171 and Asp230.

## ■ ASSOCIATED CONTENT

### ● Supporting Information

One figure showing for each simulation the contribution of individual Na<sup>+</sup> ions in occupying the Asp171 and Asp230 sodium binding sites. This material is available free of charge via the Internet at <http://pubs.acs.org>.

## ■ AUTHOR INFORMATION

### Corresponding Author

\*E-mail: [kandt@bit.uni-bonn.de](mailto:kandt@bit.uni-bonn.de). Phone: 49 228 2699 324. Fax: 49 228 2699 341.

### Present Address

<sup>†</sup>Zentrum für Bioinformatik, University of Hamburg, Bundesstraße 43, 20146 Hamburg, Germany.

### Funding

This work was financially supported by the Ministerium für Innovation, Wissenschaft und Forschung des Landes Nordrhein-Westfalen. C.K. is a junior research group leader funded by the NRW Rückkehrerprogramm.

### Notes

The authors declare no competing financial interest.

## ■ REFERENCES

- (1) Ramos, J. L., and Filloux, A. (2010) *Pseudomonas: Volume 6: Molecular Microbiology, Infection and Biodiversity*, Plenum Publishing Company Ltd., New York.
- (2) Mesáros, N., Nordmann, P., Plesiat, P., Roussel-Delvallez, M., Van Eldere, J., Glupczynski, Y., Van Laethem, Y., Jacobs, F., Lebecque, P., Malfroot, A., Tulkens, P. M., and Van Bambeke, F. (2007) *Pseudomonas aeruginosa*: Resistance and therapeutic options at the turn of the new millennium. *Clin. Microbiol. Infect.* 13, 560–578.
- (3) Putman, M., van Veen, H. W., and Konings, W. N. (2000) Molecular properties of bacterial multidrug transporters. *Microbiol. Mol. Biol. Rev.* 64, 672–693.
- (4) Strateva, T., and Yordanov, D. (2009) *Pseudomonas aeruginosa*: A phenomenon of bacterial resistance. *J. Med. Microbiol.* 58, 1133–1148.
- (5) Poole, K., Krebs, K., McNally, C., and Neshat, S. (1993) Multiple antibiotic resistance in *Pseudomonas aeruginosa*: Evidence for involvement of an efflux operon. *J. Bacteriol.* 175, 7363–7372.
- (6) Masuda, N., Sakagawa, E., Ohya, S., Gotoh, N., Tsujimoto, H., and Nishino, T. (2000) Substrate specificities of MexAB-OprM, MexCD-OprJ, and MexXY-oprM efflux pumps in *Pseudomonas aeruginosa*. *Antimicrob. Agents Chemother.* 44, 3322–3327.
- (7) Kohler, T., Michea-Hamzehpour, M., Henze, U., Gotoh, N., Curty, L. K., and Pechere, J. C. (1997) Characterization of MexE-MexF-OprN, a positively regulated multidrug efflux system of *Pseudomonas aeruginosa*. *Mol. Microbiol.* 23, 345–354.
- (8) Masuda, N., Sakagawa, E., Ohya, S., Gotoh, N., Tsujimoto, H., and Nishino, T. (2000) Contribution of the MexX-MexY-oprM efflux system to intrinsic resistance in *Pseudomonas aeruginosa*. *Antimicrob. Agents Chemother.* 44, 2242–2246.
- (9) Nakajima, A., Sugimoto, Y., Yoneyama, H., and Nakae, T. (2002) High-level fluoroquinolone resistance in *Pseudomonas aeruginosa* due to interplay of the MexAB-OprM efflux pump and the DNA gyrase mutation. *Microbiol. Immunol.* 46, 391–395.
- (10) Hancock, R. E., and Brinkman, F. S. (2002) Function of *Pseudomonas* porins in uptake and efflux. *Annu. Rev. Microbiol.* 56, 17–38.
- (11) Wong, K. K., Brinkman, F. S., Benz, R. S., and Hancock, R. E. (2001) Evaluation of a structural model of *Pseudomonas aeruginosa* outer membrane protein OprM, an efflux component involved in intrinsic antibiotic resistance. *J. Bacteriol.* 183, 367–374.
- (12) Zgurskaya, H. I., and Nikaido, H. (2000) Multidrug resistance mechanisms: Drug efflux across two membranes. *Mol. Microbiol.* 37, 219–225.
- (13) Xu, Y., Moeller, A., Jun, S. Y., Le, M., Yoon, B. Y., Kim, J. S., Lee, K., and Ha, N. C. (2012) Assembly and channel opening of outer membrane protein in tripartite drug efflux pumps of Gram-negative bacteria. *J. Biol. Chem.* 287, 11740–11750.
- (14) Zhao, Q., Li, X. Z., Srikumar, R., and Poole, K. (1998) Contribution of outer membrane efflux protein OprM to antibiotic resistance in *Pseudomonas aeruginosa* independent of MexAB. *Antimicrob. Agents Chemother.* 42, 1682–1688.
- (15) Gotoh, N., Tsujimoto, H., Nomura, A., Okamoto, K., Tsuda, M., and Nishino, T. (1998) Functional replacement of OprJ by OprM in the MexCD-OprJ multidrug efflux system of *Pseudomonas aeruginosa*. *FEMS Microbiol. Lett.* 165, 21–27.
- (16) Akama, H., Kanemaki, M., Yoshimura, M., Tsukihara, T., Kashiwagi, T., Yoneyama, H., Narita, S., Nakagawa, A., and Nakae, T. (2004) Crystal structure of the drug discharge outer membrane protein, OprM, of *Pseudomonas aeruginosa*: Dual modes of membrane anchoring and occluded cavity end. *J. Biol. Chem.* 279, 52816–52819.
- (17) Phan, G., Benabdelhak, H., Lascombe, M. B., Benas, P., Rety, S., Picard, M., Ducruix, A., Etchebest, C., and Broutin, I. (2010) Structural and dynamical insights into the opening mechanism of *P. aeruginosa* OprM channel. *Structure* 18, 507–517.
- (18) Zgurskaya, H. I., Krishnamoorthy, G., Ntrel, A., and Lu, S. (2011) Mechanism and Function of the Outer Membrane Channel TolC in Multidrug Resistance and Physiology of Enterobacteria. *Front. Microbiol.* 2, 189.
- (19) Raunest, M., and Kandt, C. (2012) Locked on one side only: Ground state dynamics of the outer membrane efflux duct TolC. *Biochemistry* 51, 1719–1729.
- (20) Berendsen, H. J. C., van der Spoel, D., and van Drunen, R. (1995) GROMACS: A message-passing parallel molecular dynamics implementation. *Comput. Phys. Commun.* 91, 43–56.
- (21) Hess, B., Kutzner, C., van der Spoel, D., and Lindahl, E. (2008) GROMACS 4: Algorithms for Highly Efficient, Load-Balanced, and Scalable Molecular Simulation. *J. Chem. Theory Comput.* 4, 435–447.
- (22) Oostenbrink, C., Villa, A., Mark, A. E., and van Gunsteren, W. F. (2004) A biomolecular force field based on the free enthalpy of hydration and solvation: The GROMOS force-field parameter sets 53A5 and 53A6. *J. Comput. Chem.* 25, 1656–1676.
- (23) Tieleman, D. P., and Berendsen, H. J. (1998) A molecular dynamics study of the pores formed by *Escherichia coli* OmpF porin in a fully hydrated palmitoylcholine bilayer. *Biophys. J.* 74, 2786–2801.
- (24) Kandt, C., Ash, W. L., and Tieleman, D. P. (2007) Setting up and running molecular dynamics simulations of membrane proteins. *Methods* 41, 475–488.
- (25) Berendsen, H. J. C., Postma, J. P. M., Van Gunsteren, W. F., and Hermans, J. (1981) Interaction models for Water in Relation to Protein Hydration. *Intermol. Forces* 11, 331–338.
- (26) Hess, B., Bekker, H., Berendsen, H. J. C., and Fraaije, J. G. E. M. (1997) LINCS: A linear constraint solver for molecular simulations. *J. Comput. Chem.* 18, 1463–1472.
- (27) Berendsen, H. J. C., Postma, J. P. M., Vangunsteren, W. F., Dinola, A., and Haak, J. R. (1984) Molecular-Dynamics with Coupling to an External Bath. *J. Chem. Phys.* 81, 3684–3690.
- (28) Darden, T., York, D., and Pedersen, L. (1993) Particle Mesh Ewald: An NLog(N) Method for Ewald Sums in Large Systems. *J. Chem. Phys.* 98, 10089–10092.

- (29) Essmann, U., Perera, L., Berkowitz, M. L., Darden, T., Lee, H., and Pedersen, L. G. (1995) A smooth particle mesh Ewald method. *J. Chem. Phys.* 103, 8577–8593.
- (30) Schulz, R., and Kleinekathofer, U. (2009) Transitions between closed and open conformations of TolC: The effects of ions in simulations. *Biophys. J.* 96, 3116–3125.
- (31) Andersen, C., Koronakis, E., Hughes, C., and Koronakis, V. (2002) An aspartate ring at the TolC tunnel entrance determines ion selectivity and presents a target for blocking by large cations. *Mol. Microbiol.* 44, 1131–1139.
- (32) Andersen, C., Koronakis, E., Bokma, E., Eswaran, J., Humphreys, D., Hughes, C., and Koronakis, V. (2002) Transition to the open state of the TolC periplasmic tunnel entrance. *Proc. Natl. Acad. Sci. U.S.A.* 99, 11103–11108.
- (33) Delano, W. L. (2002) *The PyMOL Molecular Graphics System*, DeLano Scientific, San Carlos, CA.
- (34) Fischer, N., and Kandt, C. (2011) Three ways in, one way out: Water dynamics in the trans-membrane domains of the inner membrane translocase AcrB. *Proteins* 79, 2871–2885.
- (35) Stover, C. K., Pham, X. Q., Erwin, A. L., Mizoguchi, S. D., Warren, P., Hickey, M. J., Brinkman, F. S., Hufnagle, W. O., Kowalik, D. J., Lagrou, M., Garber, R. L., Goltry, L., Tolentino, E., Westbrook-Wadman, S., Yuan, Y., Brody, L. L., Coulter, S. N., Folger, K. R., Kas, A., Larbig, K., Lim, R., Smith, K., Spencer, D., Wong, G. K., Wu, Z., Paulsen, I. T., Reizer, J., Saier, M. H., Hancock, R. E., Lory, S., and Olson, M. V. (2000) Complete genome sequence of *Pseudomonas aeruginosa* PAO1, an opportunistic pathogen. *Nature* 406, 959–964.
- (36) Lambert, P. A. (2002) Mechanisms of antibiotic resistance in *Pseudomonas aeruginosa*. *J. R. Soc. Med.* 95 (Suppl. 41), 22–26.
- (37) Piggot, T. J., Holdbrook, D. A., and Khalid, S. (2012) Conformational dynamics and membrane interactions of the *E. coli* outer membrane protein FecA: A molecular dynamics simulation study. *Biochim. Biophys. Acta* 1828, 284–293.
- (38) Piggot, T. J., Holdbrook, D. A., and Khalid, S. (2011) Electroporation of the *E. coli* and *S. aureus* membranes: Molecular dynamics simulations of complex bacterial membranes. *J. Phys. Chem. B* 115, 13381–13388.
- (39) Straatsma, T. P., and Soares, T. A. (2009) Characterization of the outer membrane protein OprF of *Pseudomonas aeruginosa* in a lipopolysaccharide membrane by computer simulation. *Proteins* 74, 475–488.
- (40) Cuesta-Seijo, J. A., Neale, C., Khan, M. A., Moktar, J., Tran, C. D., Bishop, R. E., Pomes, R., and Prive, G. G. (2010) PagP crystallized from SDS/cosolvent reveals the route for phospholipid access to the hydrocarbon ruler. *Structure* 18, 1210–1219.
- (41) Gumbart, J., Wiener, M. C., and Tajkhorshid, E. (2009) Coupling of calcium and substrate binding through loop alignment in the outer-membrane transporter BtuB. *J. Mol. Biol.* 393, 1129–1142.
- (42) Hajjar, E., Bessonov, A., Molitor, A., Kumar, A., Mahendran, K. R., Winterhalter, M., Pages, J. M., Ruggerone, P., and Ceccarelli, M. (2010) Toward screening for antibiotics with enhanced permeation properties through bacterial porins. *Biochemistry* 49, 6928–6935.
- (43) Grossfield, A., and Zuckerman, D. M. (2009) Quantifying uncertainty and sampling quality in biomolecular simulations. *Annu. Rep. Comput. Chem.* 5, 23–48.
- (44) Kandt, C., Xu, Z., and Tieleman, D. P. (2006) Opening and closing motions in the periplasmic vitamin B12 binding protein BtuF. *Biochemistry* 45, 13284–13292.
- (45) Bavro, V. N., Pietras, Z., Furnham, N., Perez-Cano, L., Fernandez-Recio, J., Pei, X. Y., Misra, R., and Luisi, B. (2008) Assembly and channel opening in a bacterial drug efflux machine. *Mol. Cell* 30, 114–121.
- (46) Pei, X. Y., Hinchliffe, P., Symmons, M. F., Koronakis, E., Benz, R., Hughes, C., and Koronakis, V. (2011) Structures of sequential open states in a symmetrical opening transition of the TolC exit duct. *Proc. Natl. Acad. Sci. U.S.A.* 108, 2112–2117.
- (47) Koronakis, V., Sharff, A., Koronakis, E., Luisi, B., and Hughes, C. (2000) Crystal structure of the bacterial membrane protein TolC central to multidrug efflux and protein export. *Nature* 405, 914–919.